HEALTH AND MEDICINE

An annular corneal microneedle patch for minimally invasive ophthalmic drug delivery

Lu Wang[1,2,3]†, Yishun Guo[4]†, Ben Chen[2,3], Si Lu[2,3], Jianhua Yang[2,3], Yingying Jin[2,3], Xinyi Wang[2,3], Xinyue Sun[2,3], Shuting Wang[2,3], Bailiang Wang[2,3]*

Microneedles directly penetrating into the cornea inevitably cause pain, corneal structure damage, and reduced light transmittance. In this work, a minimally invasive annular microneedle (A-MN) patch was developed avoiding direct puncture into the central cornea for ophthalmic drug delivery. The feasible mechanical strength of A-MNs was achieved by adjusting the ratio of PVP-β-CD and PVA to puncture the cornea barrier. Through effective diffusion to corneal stroma, bioavailability of hydrophilic small-molecule drugs, hydrophobic drugs, and macromolecular protein drugs through an A-MN patch was 24.36, 17.47, and 5.36 times higher than that of free drug administration. A-MNs effectively maintained light transmittance of the cornea with a light transmittance of 96.33 to 100%, which was higher than that of S-MNs. Furthermore, A-MNs effectively avoided corneal tissue and nerve damage along with the pain. The efficiency and safety of A-MNs were also examined through both an in vitro cell experiment and an in vivo animal experimental model, which showed great potential in clinical application.

INTRODUCTION

As the aging population increases, visual health has become an important factor restricting people's quality of life and economic status. The International Classification of Diseases-11 (2018) states that approximately 1.3 billion people live with some forms of vision impairment globally (*1*). As per the World Health Organization report, every 5 s, someone in the world goes blind, and every minute, a child loses sight. Ocular diseases are roughly divided into anterior segment diseases (corneal infections, dry eye, glaucoma, cataracts, etc.) and posterior segment diseases (age-related macular degeneration, diabetic retinopathy, uveitis, retinal vein occlusion, macular edema, etc.) based on the anatomical structure segmented by the lens. In clinical practice, medication administered in the form of eye drops plays an important role in saving patients' vision in eye disease treatment. Approximately 90% of the commercialized ophthalmic products are in the form of eye drops for clinically ocular surface and anterior chamber disease treatment due to strong operability and the least invasiveness (*2*). Ocular surface drug delivery in eye drops can basically be divided into three types of drugs: small-molecule hydrophilic drugs, hydrophobic drugs, and macromolecular protein drugs. The most diverse eye drops are hydrophilic drugs, which include antibiotics (aminoglycosides, quinolones, macrolides, etc.), hormone and nonsteroidal anti-inflammatory drugs (dexamethasone, diclofenac, indomethacin, etc.), cataract medication, intraocular pressure lowering drugs for glaucoma (bemeprost, metoprolol, etc.), and dry eye medication.

However, it is difficult for free drugs to effectively penetrate into the cornea and enter the eye due to a series of static and dynamic physiological barriers, which reduce their retention time on the ocular surface, resulting in very low bioavailability of drugs (*3*, *4*). The static physiological barriers mainly include lacrimal film, scleral barrier, cornea barrier, blood-retinal barrier, and blood-humor barrier, which restrict most of the drug penetration (*5*, *6*). These structures yield drug retention and penetration restriction mainly based on sandwich-like layers (lipid-aqueous-lipid), protein interaction, electric charges, and cell tight conjunctions (*4*). For example, the cornea is the principal path for the intraocular absorption and consists of the following 5 layers: the epithelium (hydrophobic), Bowman's membrane, the lamellar stroma (hydrophilic), Descemet's membrane, and the endothelium (hydrophobic). Dynamic physiological barriers including lacrimal flushing, aqueous humor circulation, choroidal blood flow, and mechanical shearing of blinking also obviously reduce the retention time of drugs on ocular surface (*7*). It is estimated that only 1 to 3% of the applied total dose can penetrate through the cornea after tear drainage (*8*), and a much lower level of drugs is allowed to reach the retina by an ocular anterior segment route (*9*, *10*). In the past few decades, quite a few studies have been carried out to enhance drug bioavailability and delivery efficiency (*11*). The researchers designed a variety of drug delivery platforms, such as drug-loaded contact lens (*12*), liposomes (*13*), dendrimers, polymer nanoparticles, nanosuspensions, and hydrogels (*14*) to improve the retention time and penetration of drugs into physiological barrier. Among these delivery systems, liposomes have been considered as a promising carrier with a good barrier penetration ability owing to a similar structure to a cell membrane. However, because of the instability and high synthetic costs, most of the delivery systems have not been applied yet.

The eyes and skin together constitute the contact surface between the human body and the outside world, which mainly play the role of physical barrier. The aim of microneedle patch development is to deliver drugs to the epidermis layer by strictly controlling the length of the needle without reaching the dermis layer to avoid pain and bleeding (*15*–*18*). The obvious advantage of microneedle drug delivery is to break through the physiological barrier in a minimally invasive way while avoiding the potential risk of infection and pain caused by traditional puncture injection, so patient compliance can be expected to be highly enhanced (*19*, *20*). Inspired by transdermal drug delivery, the development of transcorneal drug

[1]Affiliated Yueqing Hospital of Wenzhou Medical University, Wenzhou 325600, China. [2]National Engineering Research Center of Ophthalmology and Optometry, Eye Hospital, Wenzhou Medical University, Wenzhou 325027, China. [3]State Key Laboratory of Ophthalmology, Optometry and Visual Science, Eye Hospital, Wenzhou Medical University, Wenzhou 325027, China. [4]First Affiliated Hospital of Wenzhou Medical University, Wenzhou 325000, China.
*Corresponding author. Email: blwang@wmu.edu.cn
†These authors contributed equally to this work.

delivery system on the ocular surface may be an effective strategy to improve the ocular surface efficiency. As for ophthalmic microneedle drug delivery, several now reported drug delivery systems are directly punctured into the corneal center area for corneal and ocular surface disease treatment (*21*). For example, a microneedle patch has been used to treat corneal neovascularization by inserting microneedle patches into the cornea and directly deliver antiangiogenic antibodies into the cornea in a minimally invasive way (*21*). This advanced administration mode can greatly improve the bioavailability of drug. However, the main difference between transcorneal drug delivery and transdermal drug delivery is the need to maintain light transmittance of eye tissues on the optical path. It should be emphasized that the now reported S-MN patches for ophthalmic drug delivery through direct cornea piercing are not desirable owing to the irreversible damage to the anterior elastic layer and the stroma layer, inevitably intense pain, as well as the decrease of corneal light transmittance. Furthermore, Bowman's membrane, lamellar stroma, Descemet's membrane, and endothelium cannot be regenerated once damaged. Therefore, it is urgent to develop a new type of minimally invasive ocular surface drug delivery system to achieve efficient drug delivery while avoiding damage to corneal tissue.

Cornea is a transparent avascular tissue (about 560 μm thick) located on the anterior side of the eye. On the basis of analysis of various layers of cornea and eyeball wall, as the main structure of cornea, a stromal layer extends to the pericorneal area (*22*). Once drug is delivered to this area, it can further penetrate and diffuse to cornea, anterior chamber, and even fundus areas avoiding the adverse effects of dynamic and static physiological barriers on the ocular surface (*23*). In addition, the density of epithelial nerve endings in the cornea is about 300 to 600 times that of skin and 20 to 40 times that of dental pulp (*24*). In terms of distribution, the density of corneal nerve endings gradually decreases from the center to the periphery (*25*). Therefore, it can be inferred that the microneedle delivery system for direct corneal puncture reported in the literature inevitably causes severe pain. On the other hand, low local drug concentration in eye drop delivery mode greatly reduces overall delivery efficiency and limits the effect of disease treatment. For example, in treating persistent intractable keratitis, the fourth leading cause of blindness after cataracts, glaucoma, and age-related macular degeneration (*1*, *26*), the low drug delivery efficiency and insufficient local antibiotic concentration cause bacterial biofilm formation and drug resistance development. Once corneal tissue is damaged, the repair process will still cause new blood vessels and scarring even if bacteria are completely killed. The integrity of the central cornea is essential in maintaining vision, and the damage to the central cornea should be avoided in treating ocular surface diseases. On the basis of the minimally invasive characteristics of microneedles, the development of annular corneal margin microneedles may be an effective strategy to achieve effective drug delivery into the anterior segment while avoiding mechanical damage to the central corneal region (*27*).

In this work, we proposed a strategy of annular pericorneal microneedle patches for effective drug delivery into the anterior segment. To construct the microneedle patches, biodegradable polymer materials polyvinylpyrrolidone–β-cyclodextrin (PVP-β-CD) and polyvinyl alcohol (PVA) are selected to prepare soluble drug-loaded annular microneedles (A-MNs) through simple centrifugation or vacuum methods. The degradation, mechanical strength, and drug release behavior of A-MNs after loading hydrophilic drugs, hydrophobic drugs, and macromolecular drugs are examined in detail. The light transmission of cornea after A-MN puncturing into the pericoreal area is compared with that after square microneedle (S-MN) puncturing into the central cornea. To verify in vivo distribution and bioavailability of drugs, fluorescein isothiocyanate (FITC), chlorin e6 (Ce6), and FITC-grafted bovine serum albumin (BSA-FITC) are selected as model drugs for fluorescence observation. As a proof of concept, a bacterial keratitis animal model is used to verify the antibacterial drug delivery efficiency of A-MNs in corneal disease treatment. It is believed that A-MNs showed great potential in ophthalmic drug delivery owing to the independence of drug types, adjustable drug loading dosage, optical pathway protection, and corneal barrier penetration in a minimally invasive way.

RESULTS

Preparation and characterization of A-MN patch

The preparation method of A-MNs is shown in Fig. 1A, in which different drugs were mixed with needle matrix solution for microneedle preparation in advance. S-MNs were prepared by injection molding and then cut into an A-MN patch with an inner diameter 4.5 mm and an outer diameter 8.5 mm for rat cornea, while inner and outer diameters were set to 6 and 10 mm for rabbit cornea. The length of needle was set to 400 μm to just reach the depth of the corneal stroma layer. The corresponding mold was constructed through microfabrication technology. As shown in Fig. 1B, the main goal of A-MN design is to address the low bioavailability issue of eye drops, as well as severe pain and reduced light transmittance caused by now reported S-MN patches. The A-MNs avoid the central area of the cornea that is rich in nerve endings for painless drug delivery. It can deliver different types of drugs horizontally to the corneal stroma layer and vertically to the anterior chamber, mainly for ocular surface and anterior segment disease treatment. To protect the patient's visual function, this minimally invasive drug delivery mode avoids damage to the corneal central area where the main optical pathway passes. In the application of anterior segment disease treatment, infectious keratitis serves as a disease model to test the role of A-MNs in drug delivery compared with clinically used antibiotic eye drops. The focus is on bactericidal efficiency, inflammation clearance, neovascularization, and corneal scar formation examination after wound healing, which highly affect corneal transparency (Fig. 1C).

Cornea is the most densely distributed tissue of nerves in human body, with free nerve endings of approximately 7000/mm^2. The nerve bundles originating from the ophthalmic branch of trigeminal ganglion form multiple branches after passing through the ciliary ganglion, reach the corneal limbus, and demyelinate after entering corneoscleral limbus for 1 mm. Wrapped by a Schwann cell, the nerve bundles shaped in the corneal stroma 293 ± 106 μm away from the eye surface. After vertically passing through the Bowman's layer, the subbasal nerve plexus forms between the basal part of the corneal epithelium and the Bowman's layer to support the corneal epithelium. The four layers of cells near the base of the epithelium are innervated by nerves. In addition to the corneal nerves that enter the sclera, there are also nerves originating from the subconjunctival tissue, which surround the corneal limbus at a distance of approximately 1.5 mm and form a paralimbal plexus distributed between the epithelial layer and the stromal layer. So the cornea is

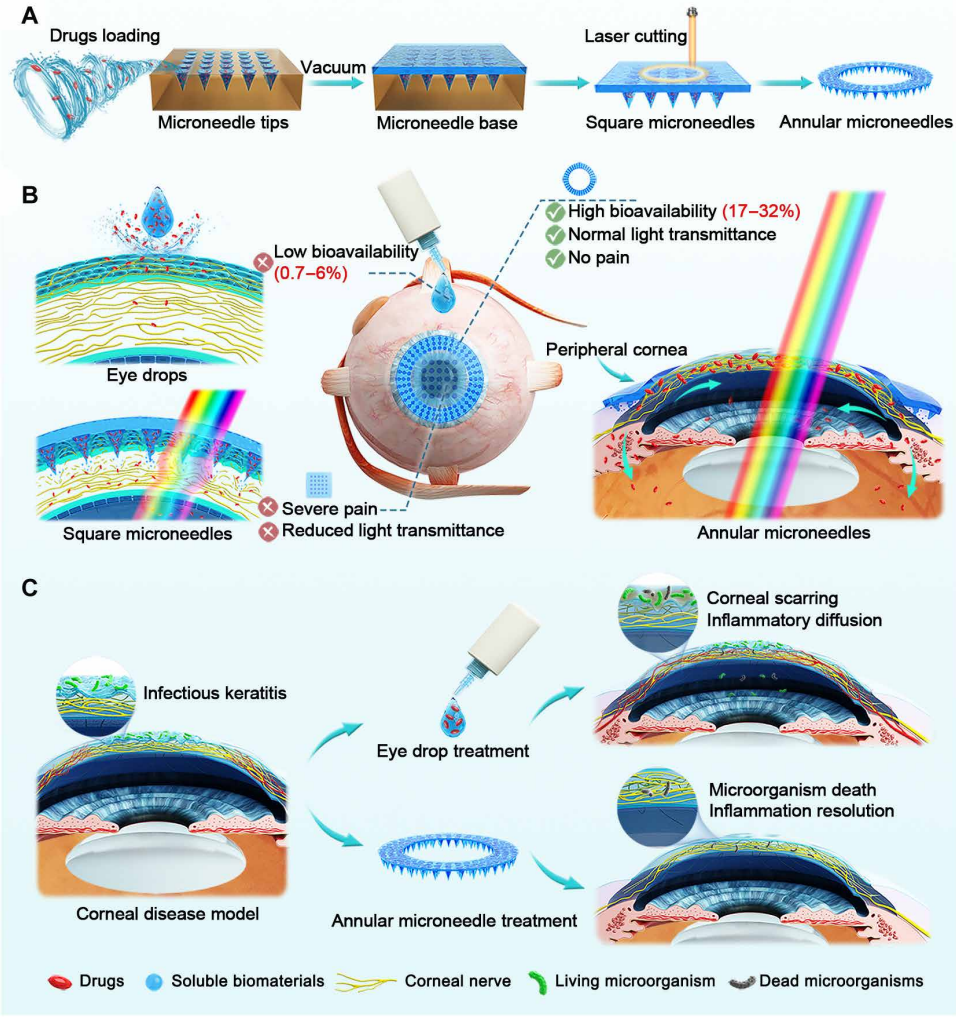

Fig. 1. Schematic illustration of annular microneedle (A-MN) characteristics and its application in treating corneal diseases. (**A**) Drug loading and molding process of A-MNs. (**B**) Advantage and disadvantage comparison of several ocular surface drug delivery modes. (**C**) The effect of A-MNs in ophthalmic disease treatment.

the area with the most nerve endings in the body, and its perception is the most acute. Therefore, the specially designed mold gives the needle a conical shape for easy penetration into the tissue, and the needle is designed at 400 μm in height and 1 mm from the corneal edge to avoid reaching the area of capillary plexus and limbal stem cells (Fig. 2A). The precursor fluid of microneedle matrix loaded with various drugs (hydrophilic drugs, hydrophobic drugs, and protein macromolecule drugs) was poured into the mold to remove gas from the mold through a simple vacuum method for a full needle body. The S-MN patch after natural drying was used to obtain an A-MN with a target size through laser cutting technology for programmed settings.

As shown in Fig. 2B, after laser cutting, the boundary of circular microneedle was clear with needle bodies evenly distributed on one side of the patch. In addition, the inner and outer diameters of the patch size could be further designed and adjusted as needed. The drug loading amount could be adjusted as needed during precursor fluid preparation. In particular, after loading hydrophobic drugs, drugs were evenly distributed within the patch (including needle body and matrix) (Fig. 2C). As observed by scanning electron microscopy (SEM), the synthesized A-MNs were uniformly distributed on the substrate in a conical shape with a needle height at ~400 μm (Fig. 2, D and E). Then, the mechanical strength of A-MN patch was subjected to top-down compression testing using a universal testing machine (Fig. 2F). Two compression modes were used to test the mechanical strength of individual A-MN patch and that when entering the detached cornea, respectively (Fig. 2G). The upper part showed that an A-MN patch was directly placed flat on the working table, and a pressure device was applied to press downward from top to bottom after touching the needle tip. The lower part showed that the detached cornea was fixed on a working table supported by a mold made of agar gel below the cornea. Then, the pressure device with the lower side attached an A-MN patch by double-sided adhesive was pressed downward the cornea, and pressure changes were recorded during the process penetrating into cornea. As shown in Fig. 1H, after compression, all needle bodies of A-MNs disappeared and fused with the basal layer, indicating a complete compression process.

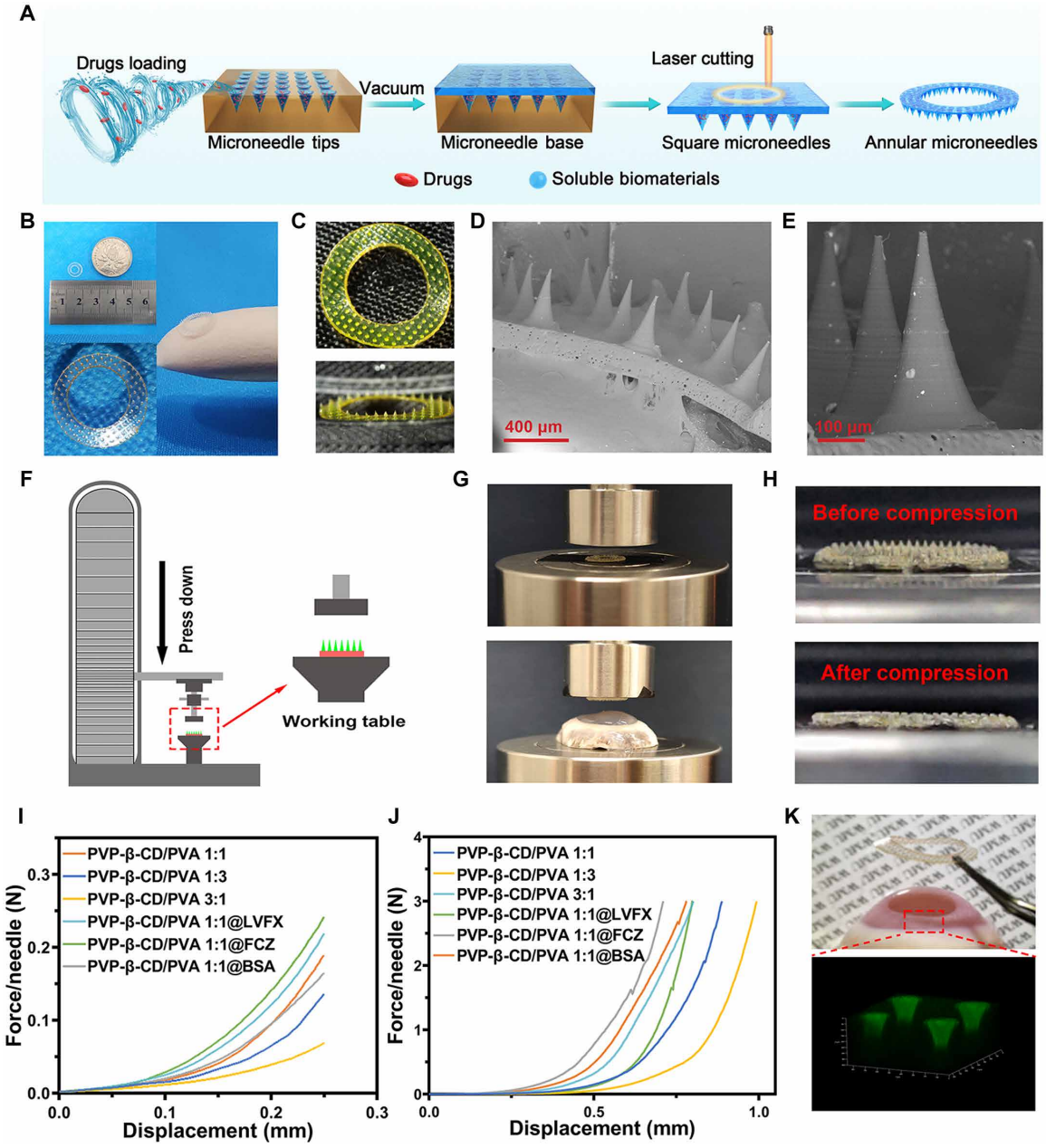

Fig. 2. Characterizations of annular microneedles (A-MNs). (**A**) Schematic illustration of A-MN fabrication. (**B**) The bright-field image of A-MNs, the size of A-MNs using a ruler compared with a coin. (**C**) Orthographic and side view of A-MNs after loading of FITC. (**D**) SEM images of A-MNs. Scale bar, 400 μm. (**E**) SEM images of a single needle in A-MNs. Scale bar, 100 μm. (**F**) Schematic diagram of universal testing machine. (**G**) In a physical test, a compression probe moves down to compress the A-MNs to insert into an isolated porcine cornea. (**H**) The changes of needle bodies before and after compression. (**I**) The changes of forces that bending and crushing A-MNs as the increase of displacements before and after LVFX, FCZ, and BSA loading. A-MNs were made up of with different ratios of 20 wt % PVP-β-CD and 10 wt % PVA (1:1, 1:3, and 3:1). (**J**) The changes of forces needed for A-MNs before and after drug loading when inserted into a porcine cornea with different ratios of 20 wt % PVP-β-CD and 10 wt % PVA (1:1, 1:3, and 3:1). (**K**) Confocal images of A-MNs when inserting into a rabbit cornea.

As shown in Fig. 2I, the A-MNs made of 20 wt % PVP-β-CD and 10 wt % PVA mixed solution at the ratio of 1:1 required the greatest force to produce displacement, indicating the greatest mechanical strength of microneedles. Furthermore, at such ratio, three kinds of A-MNs loaded with levofloxacin (LVFX), fluconazole (FCZ), and BSA, respectively, all exhibited a mild enhancement of mechanical strength. As shown in Fig. 2G, the forces needed for the A-MNs to pierce into the porcine cornea before and after drug loading were also examined through a universal testing machine. The position where the transient crease existed was the moment when it pierced into the cornea. As shown in Fig. 2J, the A-MNs made of PVP-β-CD and PVA at the ratio of 1:1 showed a transient crease when the force reached 2.05 N, indicating that microneedles were able to be pierced into porcine cornea. However, A-MNs at the ratios of 1:3 and 3:1 did

not show any crease in the mechanical curves, indicating that both microneedles failed to pierce into porcine cornea. The needle body was too flexible with a high content of PVA in A-MNs at the ratio of 1:3, resulting in a decrease in mechanical strength, while A-MNs at the ratio of 3:1 had more PVP-β-CD content and dissolved too quickly, resulting in insufficient time to penetrate into cornea. In addition, A-MNs loaded with different kinds of drugs at the ratio of 1:1 also pierced into the porcine cornea with even higher mechanical strength than drug-free microneedles and proper swelling when contacting cornea. The morphology of an FITC-labeled needle after penetrating into the cornea was also observed through a laser confocal microscope. As shown in Fig. 2K, the needle body remained intact in the corneal limbus tissue, indicating the adequate mechanical strength of the needle body for puncture. As the needle body dissolved, the drug was released into the tissue, and the pore structure generated by puncture also provided a channel for further drug diffusion into cornea.

Furthermore, the loading and distribution of various drugs into A-MNs were characterized by fluorescence microscopy observation. Among them, rhodamine B (RhB) and FITC with fluorescence represented hydrophilic small-molecule drugs, while Ce6 and FITC-labeled BSA represented hydrophobic drugs and macromolecular protein drugs, respectively (figs. S1 to S3). As indicated in Fig. 3A, all types of drugs could be evenly distributed within the needle body, which was basically full without needle tip defects. It is well known that PVP is commonly used as a matrix material to make instant microneedles due to its strong hydrophilicity. Therefore, three microneedles at different ratios of PVP-β-CD and PVA (volume ratios: 1:1, 3:1, and 1:3) were synthesized for dissolution rate testing through puncture of A-MNs into a nutrient agar plate to simulate a corneal hydration environment. As shown in Fig. 3B, under the microscope, it was observed that when the volume ratio of PVP-β-CD and PVA was 3:1, needle bodies were completely dissolved in 5 s. When the volume ratio of PVP-β-CD to PVA was 1:3, the needle remained intact all the time showing low water absorption and slow degradation property, which was also not fit for drug delivery. When the volume ratio of PVP and PVA was 1:1, the needle body underwent obvious dissolution 5 s after insertion and steadily dissolved 50% of the height in 20 s, ensuring the penetration of the needle body into the cornea and further diffused within the tissue.

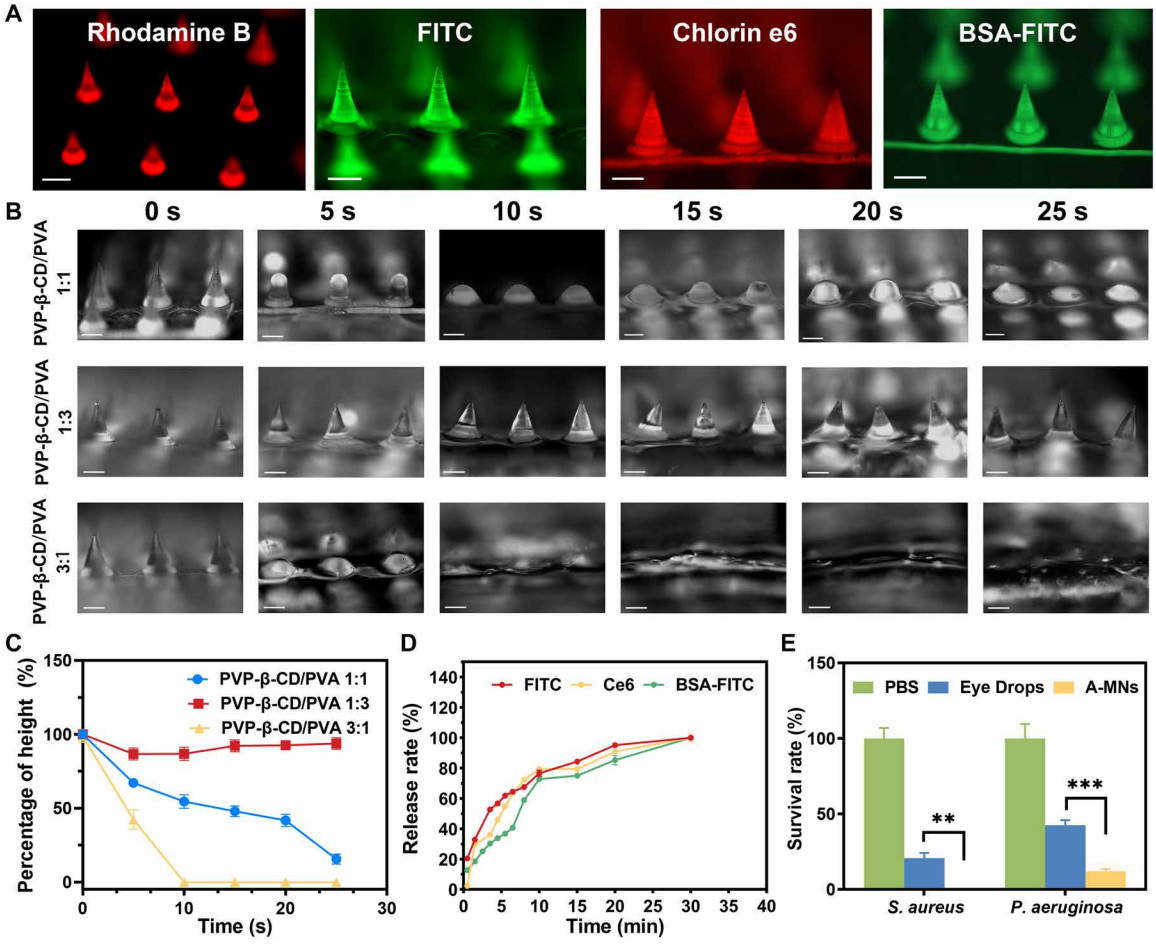

Fig. 3. Solubility, drug loading, and in vitro drug release of annular microneedles (A-MNs). (**A**) A-MNs loaded with RhB, FITC, Ce6, and FITC-grafted BSA. Scale bars, 400 μm. (**B**) Images of the dissolving A-MNs made of 20 wt % PVP-β-CD and 10 wt % PVA at different ratios (1:1, 1:3, and 3:1) in the nutrient agar plate at 0, 5, 10, 15, 20, and 25 s. Scale bars, 400 μm. (**C**) Percentage of height measured during the dissolving of different A-MNs. (**D**) The release of FITC, Ce6, and BSA from A-MNs. (**E**) Survival rates of *S. aureus* and *P. aeruginosa* after incubation with the corneal grinding fluid supernatant ($n = 3$). Data are presented as means ± SD, $n \geq 3$, and significances are determined by one-way ANOVA with Tukey's correction. $^{**}P < 0.01$ and $^{***}P < 0.001$.

The measurement of microneedle height further confirmed instant solubility of A-MN patch at a 3:1 volume ratio of PVP-β-CD/PVA and low solubility at a 1:3 volume ratio of PVP-β-CD/PVA (Fig. 3C). While the microneedles at a ratio of PVP-β-CD and PVA at 1:1 showed appropriate stability in an aqueous environment for sustained release of drugs. The drug release behavior of FITC, Ce6, and BSA-FITC from an A-MN patch was studied at a 1:1 volume ratio of PVP-β-CD/PVA. As shown in Fig. 3D, all three drugs mainly completed drug release within 30 min. The release behavior was basically not affected by types of drug but was mainly depended on the solubility of needles.

The basic requirement for A-MNs as an ophthalmic drug carrier platform is effective puncture of corneal tissue and prolonged drug retention. Antibiotic LVFX was loaded into A-MNs and inserted into the isolated porcine cornea limbus in vitro for 5 min. After grinding of corneal tissue, drug solution was extracted and cultured in contact with bacterial solution for antibacterial activity evaluation. The eye drop group with the same amount of LVFX was administered by dropwise, followed by the same subsequent treatment. As shown in Fig. 3E, the A-MN treatment group basically killed all *Staphylococcus aureus*, while about 20.81 ± 3.43% of *S. aureus* survived in the eye drop group (fig. S4). The A-MN treatment group also exhibited excellent bactericidal performance against *Pseudomonas aeruginosa*, which was superior to eye drop treatment. Therefore, compared with eye drops, minimally invasive circular microneedle delivery mode achieved better drug delivery into cornea.

Biosafety comparison between A-MNs and S-MNs

The safety of A-MN patch was compared with the reported S-MN patch that was directly punctured into central corneas of rats, including structural damage to cornea, transparency, nerve damage, etc. As shown in Fig. 4A, corneal tissue has no blood vessels but has abundant nerve endings at a high density especially in the central area. It should be noted that peripheral nerves run from a deep matrix layer to the center, and nerve endings in the center of the cornea are mainly distributed in the epithelial layer, the anterior elastic layer, and the shallow corneal stroma layer of the cornea (*28*), which is exactly the puncture area of the reported S-MN microneedle. So nerve injury is an inevitable issue of S-MN puncture in the central corneal area. As shown in Fig. 4 (B and C), the central nerve endings of the normal cornea stained using anti–β-III tubulin of mice were distributed in a vortex shape. However, after S-MN puncture, the central nerve endings in the cornea showed obvious rupture and became sparse in distribution. In comparison, most of the central nerve endings of the cornea after A-MN puncture were still continuously distributed in a vortex shape. Therefore, direct puncture of the central corneal region inevitably caused severe pain, highly reducing the possibility of clinical application.

As shown in Fig. 4D, two types of microneedle patches with the same needle body and drug loading were observed under a slit lamp after in vivo corneal puncture. The central area of the cornea punctured by A-MNs was clear and transparent without an obvious inflammatory response. In contrast, the central area of the cornea after punctured by S-MNs was filled with holes, indicating the obvious damage of cornea. After sodium fluorescein labeling, it further visually displayed that the holes treated by A-MNs and S-MNs were distributed in the limbus and the central area of corneas, respectively. Furthermore, corneal tissue was sectioned for hematoxylin and eosin (H&E) staining, which showed that the central area of the cornea treated by A-MNs was smooth without an obvious damage (Fig. 4E). Cornea treated by S-MNs showed an obvious damage to the corneal epithelium and the anterior elastic layer in the central area of cornea, and thickness of the punctured corneal area obviously increased, indicating inflammatory reaction of the cornea in a swollen state. As for the transparency of corneas after puncture of different microneedle patches, the punctured corneas were visually observed on color logo, black logo, and gauze backgrounds (Fig. 4F). It was found that corneal transparency in the A-MN–treated group was close to that of unpunctured normal cornea. A distinct decrease in corneal transparency visible to the naked eye after S-MN puncture might be because of the destruction of the corneal epithelial cell layer, the dense preelastic layer, and the fiber structure.

Furthermore, corneal transparency was quantitatively tested under ultraviolet-visible spectroscopy after puncture of different microneedle patches. As shown in Fig. 4G, after A-MN punctured corneal margin, the cornea basically maintained its high transparency compared with normal cornea. After S-MN puncture, corneal transparency in the entire visible light range obviously decreased, especially in the low wavelength range. Changes of corneal thickness directly demonstrated the inflammatory response status of cornea. After corneal injury, inflammation, edema, and turbidity highly led to a distinct increase in corneal thickness. As shown in Fig. 4H, there was no obvious change of central cornea thickness after A-MN puncture, indicating that corneal limbal puncture did not cause a distinct central corneal damage and an inflammatory response. On the contrary, central corneal thickness increased 12.0 ± 6.8 μm after S-MN puncture compared to that of normal cornea, indicating distinct edema of cornea.

When the cornea undergoes mechanical stimulation, it elicits the activation of pain receptors and subsequent release of chemokines including cyclooxygenase 2 (COX2), interleukin-8 (IL-8), IL-1β, IL-6, etc. Among these molecules, IL-8 interact with G protein–coupled receptor CXCR2 to recruit downstream signaling proteins and initiate second messenger–mediated signal transduction, thereby inducing pain sensation (*29*). As depicted in Fig. 5 (A to D), upon insertion into cornea, A-MNs and S-MNs exhibited higher expression levels of COX2 and CXCR2 in the S-MN group than that in the A-MN group. Consistently, similar trends of the mRNA level were also observed with significant up-regulation of IL-8, COX2, IL-1β, and IL-6 transcripts in the S-MN–treated group (Fig. 5, E to H). Furthermore, the biocompatibility of A-MNs was also examined through both in vitro and in vivo tests. First, cytotoxicity of A-MNs was evaluated by Cell Counting Kit-8 (CCK-8) assay toward human corneal epithelial cells (HCECs). As shown in fig. S5, A-MNs made of different ratios of PVP-β-CD and PVA all exhibited high cell survival indicating low cytotoxicity. A-MNs made of 10 wt % PVA showed low cell survival of 88.49 ± 2.52% as compared to 20 wt % PVP-β-CD. Furthermore, A-MNs made of PVP-β-CD and PVA at the ratios of 1:1 and 3:1 showed increased cell viability up to 104.80 ± 4.85% and 108.80 ± 7.72%, respectively. After loading LVFX (5 mg/ml), LVFX (10 mg/ml), and FCZ (5 mg/ml), A-MNs also showed high cell viability.

In vivo biocompatibility and an inflammatory response were studied to compare the safety of minimally invasive drug delivery mode of A-MNs and S-MNs. Different modes were administered on

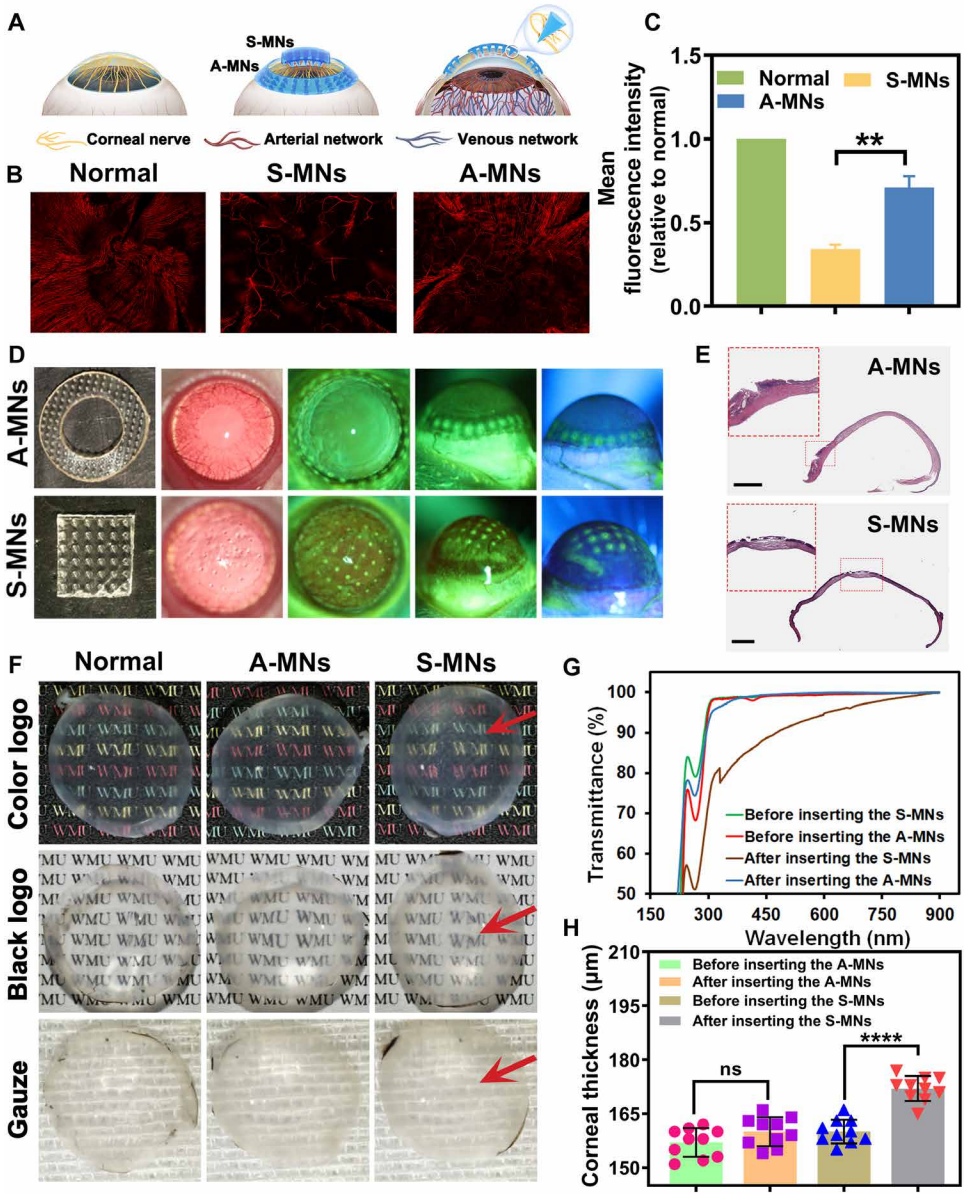

Fig. 4. Effects of annular microneedles (A-MNs) and square microneedles (S-MNs) on cornea. (**A**) Schematic diagram of the effect of A-MN and S-MN puncture on corneal nerves and blood vessels. (**B** and **C**) Distribution and semiquantitative analysis of relative mean fluorescence intensity of corneal nerves after A-MN and S-MN puncture. (**D**) Bright-field images and cobalt blue light mode images after S-MNs and A-MNs inserting into corneas of rats under a silt lamp. (**E**) H&E staining micrographs of corneas after S-MN and A-MN puncture. Scale bars, 200 μm. (**F**) Images of corneas in each group on the black paper with colorful logos and white paper with black logos and gauze. Red arrows mark the blurred and damaged areas. (**G**) The corneal transparency before and after S-MN and A-MN puncture. (**H**) Corneal central thickness before and after S-MN and A-MN puncture ($n = 10$). Data are presented as means ± SD, $n \geq 3$, biological replicate, and significances are determined by one-way ANOVA with Tukey's correction. $^{**}P < 0.01$ and $^{****}P < 0.0001$. ns, not significant.

rat corneas every day for 7 days. As shown in Fig. 6A, the cornea showed good transparency under slit lamp observation for 7 days in the control group without microneedle puncture, as well as those in A-MN– and A-MNs@LVFX–treated groups. There was no obvious conjunctival congestion, corneal turbidity, and anterior chamber inflammatory irritation. Only in the group punctured by S-MNs, distinct conjunctival congestion, swelling, and decreased transparency occurred 3 days after puncture, indicating a clear inflammatory state of cornea. The conjunctival edema and congestion, corneal edema, anterior chamber exudation, and iris congestion were also evaluated according to anterior segment inflammation scores (table S1) (*30*, *31*). It scored 1.67 ± 0.58, 2.00 ± 0.00, and 2.00 ± 0.00 on the third, fifth, and seventh day in the S-MN–treated group, which were higher than that in the A-MN–treated group (fig. S6). Furthermore, a TUNEL (terminal deoxynucleotidyl transferase–mediated deoxyuridine triphosphate nick end labeling) reagent kit was used to detect the apoptosis of corneal cells. As shown in Fig. 6B, the cornea after S-MN puncture was uneven with a rough structure, and the

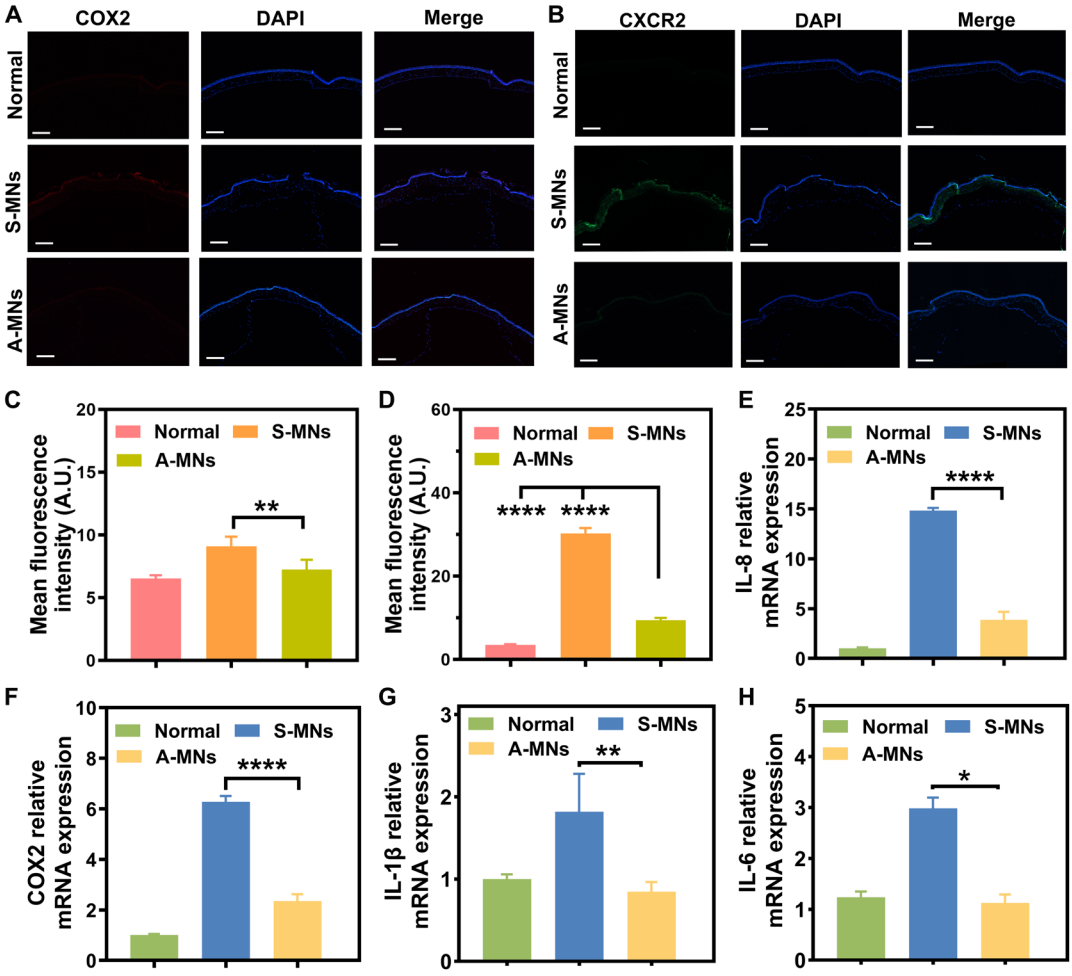

Fig. 5. Detection of pain factor expression. (**A**) Immunofluorescence images of COX2 in SD rat corneal tissues after square microneedle (S-MN) and annular microneedle (A-MN) puncture. (**B**) Immunofluorescence images of CXCR2 in SD rat corneal tissues after S-MN and A-MN puncture. (**C** and **D**) Fluorescence intensity analysis of COX2 and CXCR2 in rat corneal tissues after S-MN and A-MN puncture. (**E** to **H**) qRT-PCR analysis of IL-8, IL-1β, COX2, and IL-6 mRNA levels in rat corneal tissues after S-MN and A-MN puncture ($n = 3$). Data are presented as means ± SD, $n \geq 3$, biological replicate, and significances are determined by one-way ANOVA with Tukey's correction. *$P < 0.05$, **$P < 0.01$, and ****$P < 0.0001$. DAPI, 4′,6-diamidino-2-phenylindole; A.U., absorbance units.

corneal epithelial cell layer showed obvious green fluorescence, indicating distinct apoptosis of corneal epithelial cells. In comparison, corneal morphology in A-MN and A-MN@LVFX puncture groups was smooth without obvious defects and green fluorescence, indicating a good survival state of cells in corneal tissue. After corneal puncture, corneal epithelial cells could repair the microneedle puncture area to a certain extent through proliferation and migration, but the damaged anterior elastic layer and the corneal stroma layer did not repair owing to the irreversible formation of the regular structure (*32*). The H&E observation revealed the formation of a large number of pore structures in the stromal layer of the cornea which was the main reason for the corneal transparency decrease (Fig. 6C). In the normal cornea group and A-MN and A-MNs@LVFX puncture groups, the corneal stroma layer showed clear texture and a complete structure with a dense distribution of collagen fibers.

To further study the long-term safety of microneedles, microneedle administration was suspended after 7-day treatment to observe corneal epithelial repair and healing in corneal recovery through corneal fluorescein staining. On the 10th day, the corneal fluorescein staining score of rats in the A-MN–treated group was 0.50 ± 0.58, which was lower than that in the S-MN–treated group (4.25 ± 0.50). On the 14th day, the corneal fluorescein staining score of rats in the A-MN–treated group returned to 0, while the score in the S-MN–treated group was still up to 2.50 ± 0.58 (fig. S7 and table S2). The expressions of representative proinflammatory cytokines including IL-1β and tumor necrosis factor–α (TNF-α) were further determined by measuring mRNA expression by the quantitative reverse transcription polymerase chain reaction (qRT-PCR) method in the corneal tissue after puncture (Fig. 6, D to F). It was found that the expressions of IL-1β and TNF-α cytokines in the A-MN–treated group did not increase without a significant difference compared to the normal cornea on the 14th day. However, the expressions of IL-1β and TNF-α cytokines in the S-MN–treated group greatly increased showing the intensified inflammatory response which might be attributed to damage to corneal epithelial cells and nerve fiber endings. The expression of α-smooth muscle actin (α-SMA) protein reflects the activity of collagen fibers during corneal scar formation after corneal inflammation. On the

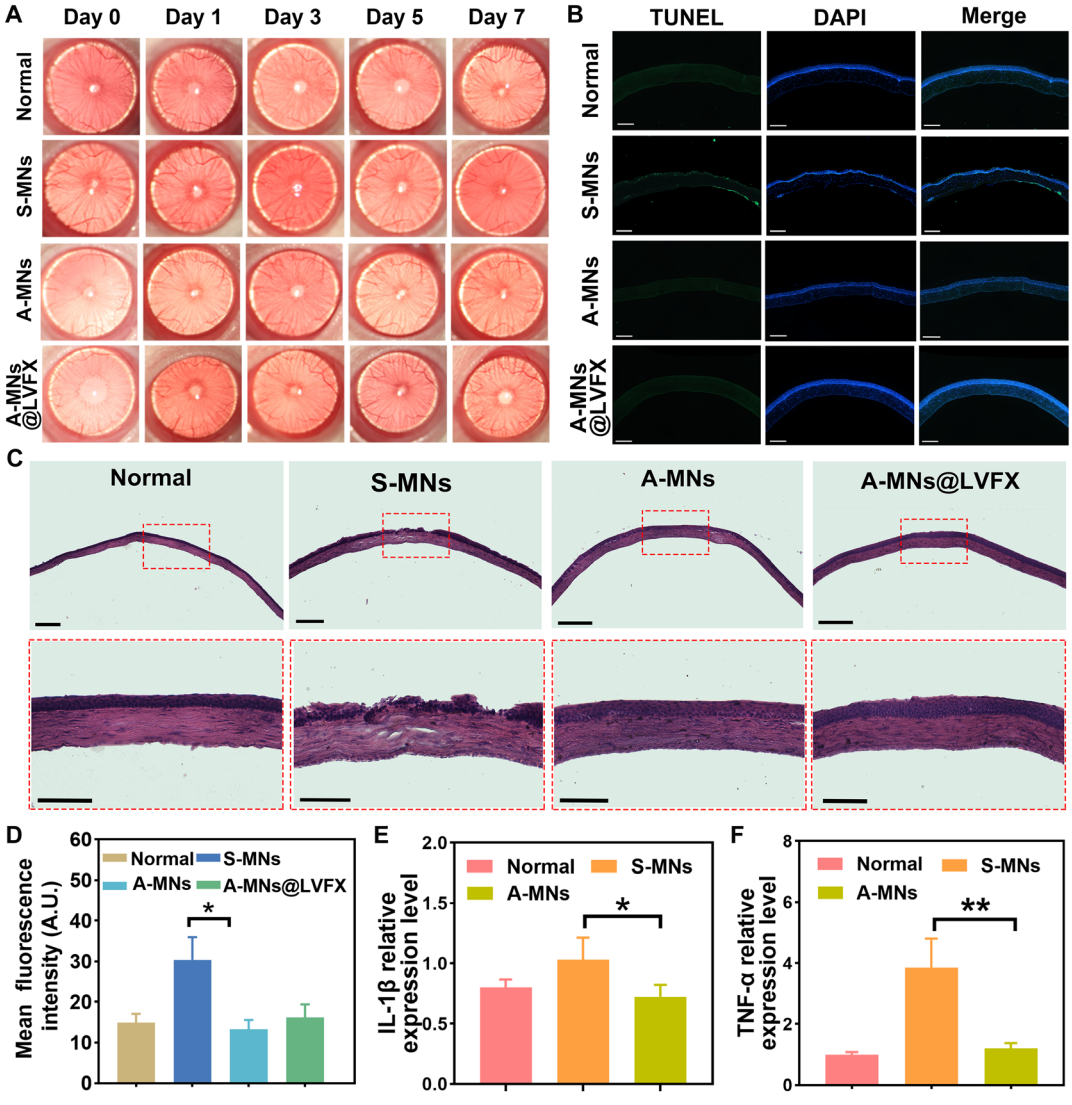

Fig. 6. In vivo biocompatibility of annular microneedles (A-MNs). (**A**) Images of rat corneas before and after square microneedle (S-MN), A-MN, and A-MNs@LVFX puncture under silt lamp microscopy. (**B**) Cell apoptosis of corneal tissues after S-MN, A-MN, and A-MNs@LVFX puncture by a TUNEL apoptosis detection kit. (**C**) Images of corneal structures after S-MN, A-MN, and A-MNs@LVFX puncture after H&E staining. Scale bars, 200 μm. (**D**) Semiquantitative analysis of relative mean fluorescence intensity of green fluorescence in TUNEL apoptosis detection. (**E**) IL-1β and (**F**) TNF-α levels in rat corneas after S-MN and A-MN puncture ($n = 3$). Data are presented as means ± SD, $n \geq 3$, biological replicate, and significances are determined by one-way ANOVA with Tukey's correction. $^{*}P < 0.05$ and $^{**}P < 0.01$.

14th day, the expression of α-SMA obviously increased in the S-MN–treated group, indicating that the cornea in the S-MN group was in a state of scarring. While α-SMA expression in the A-MN–treated group was close to that in the normal group (fig. S8).

Drug delivery efficiency of A-MNs

In subsequent study, hydrophilic drug, hydrophobic drug, and macromolecular protein drug delivery from A-MNs was compared with eye drops. The detention time of drugs on the ocular surface is a key factor affecting drug bioavailability. The retention time of fluorescein sodium–loaded A-MNs in a corneal region was observed under a slit lamp for 30 min with 1% fluorescein sodium in eye drop as control. It was found that a large area of green fluorescence covered the entire cornea at the beginning in the eye drop group, which basically disappeared after 5 min (Fig. 7A). However, in the A-MN group, it was observed that fluorescein sodium still covered the entire cornea in a uniform distribution even after 30 min. This is because fluorescein sodium gradually diffused into the corneal stroma layer from microneedles for a much longer residence time. Further statistical analysis was conducted on intensity of fluorescein sodium, and it was found that the retention time of drug in the A-MN group was more than 9.47 times than that in the eye drop group at 30 min (Fig. 7B). Furthermore, FITC, Ce6, and BSA-FITC with a fluorescence feature were loaded into A-MNs to simulate hydrophilic, hydrophobic, and protein drugs, respectively, to study drug bioavailability compared to corresponding eye drops. As shown in Fig. 7C, bioavailability of FITC, Ce6, and BSA-FITC in the A-MN group were 28.16 ± 4.27%, 23.40 ± 5.83%, and 22.04 ± 5.02%, respectively, which were 24.36, 17.45, and 5.36 times higher than that in the corresponding eye drop groups (1.16 ± 0.40%, 1.34 ± 0.15%, and 4.11 ± 1.44% for

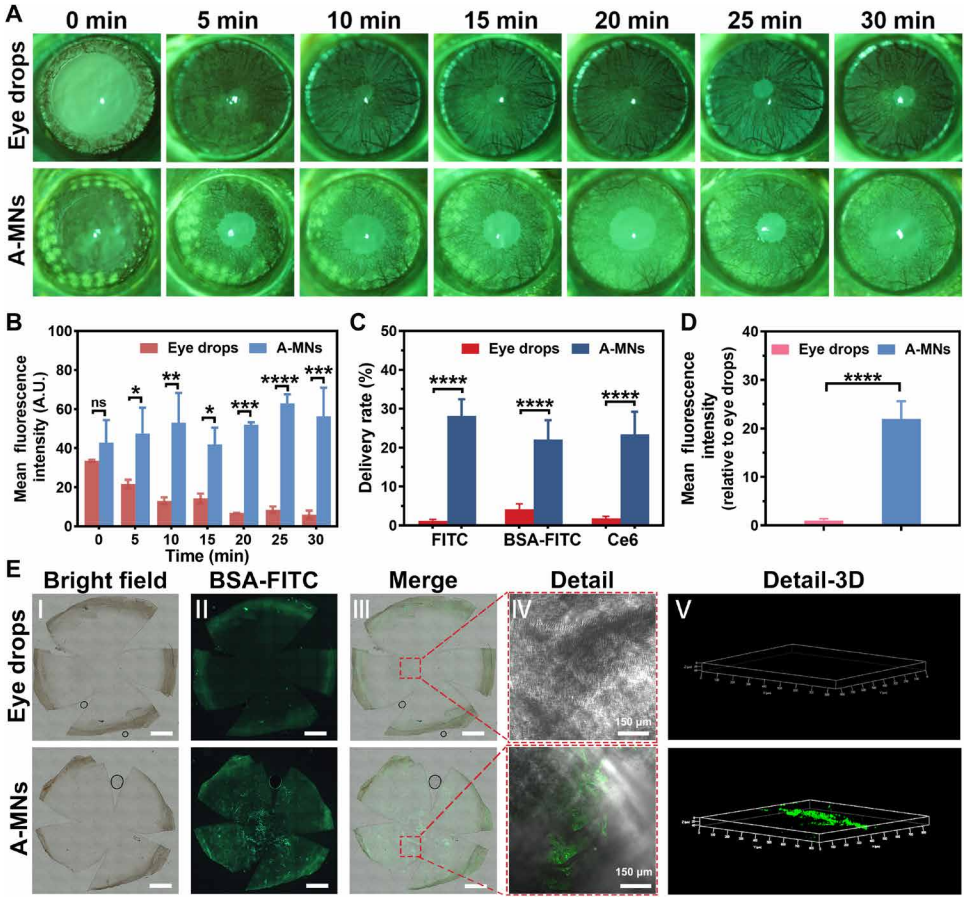

Fig. 7. Bioavailability of annular microneedles (A-MNs) compared with eye drops. (**A**) In vivo observations of the distribution of sodium fluorescein in rat eyes after A-MN puncture and eye drop administration under a silt lamp at 0, 5, 10, 15, 20, 25, and 30 min. (**B**) Semiquantitative analysis of relative mean fluorescence intensity of sodium fluorescein in rat eyes. (**C**) Bioavailability of A-MNs loaded with FITC, Ce6, and BSA-FITC in a rabbit cornea compared to eye drop with the same amount of drugs. (**D** and **E**) Confocal images and corresponding statistical analysis of corneal patches after A-MN puncture loaded with BSA-FITC and eye drop administration loading the same amount of BSA-FITC for 30 min. I to V represents the representative bright-field images of corneal patches, fluorescence distribution images of BSA-FITC, merged images, local detail images of III, and three-dimensional (3D) images of local detail, respectively. Data are presented as means ± SD, $n \geq 3$, biological replicate, and significances are determined by one-way ANOVA with Tukey's correction. *$P < 0.05$, **$P < 0.01$, ***$P < 0.001$, and ****$P < 0.0001$.

FITC, Ce6, and BSA-FITC, respectively). To observe drug distribution after entering cornea, corneas treated by A-MNs and eye drop were placed on slides (Fig. 7, D and E, and fig. S9). Under a laser confocal microscope, almost no green fluorescence could be observed in the eye drop group. However, it could be detected that the corneal stroma layer treated by A-MNs still exhibited much higher green fluorescence intensity even at 30 min with a fluorescence intensity 21.98 times that of eye drops.

In vivo infectious keratitis treatment

Infectious keratitis is a major blinding eye disease, and its treatment is mainly limited by short retention time of free antibiotic eye drops on the ocular surface. In particular, when bacteria cannot be timely killed, prolonged healing of infectious ulcer leads to bacterial progression into the corneal stroma layer, as well as severe inflammatory reaction and corneal tissue damage. Therefore, it is crucial to effectively deliver antibacterial drugs into the corneal stroma layer to increase drug bioavailability. In this work, drugs were loaded in the form of microneedle patches to penetrate into the peripheral cornea in a minimally invasive manner. Therefore, an infectious keratitis animal model was established to verify whether the constructed A-MN patch could effectively deliver drug to lesion site. As shown in Fig. 8A, within 7 days of treatment, inflammatory response status and corneal transparency were observed under a slit lamp compared with untreated cornea, A-MN–, and LVFX eye drop–treated groups. On the first day after treatment, corneal transparency in the A-MNs@LVFX–treated group was improved, which was better than those in the other three control groups. On the fifth day after treatment, corneal transparency in the A-MNs@LVFX–treated group had basically returned to that before modeling, while there were large corneal ulcers on corneas in A-MN– and LVFX eye drop–treated groups. On the seventh day, the end of the treatment cycle, corneal inflammation and ulceration still existed in A-MN– and LVFX eye drop–treated groups. At the visible light wavelength of 480 nm, the corneal transparency in the A-MNs@LVFX–treated group was 83.25 ± 0.42% on the seventh day, which exhibited a much higher value compared to that in the untreated group (52.26 ± 8.60%), the blank A-MN group (66.67 ± 1.55%), and the LVFX eye drop–treated group (71.18 ± 2.93%). Similar results were also shown at visible light wavelengths of 520 and 680 nm (fig. S10).

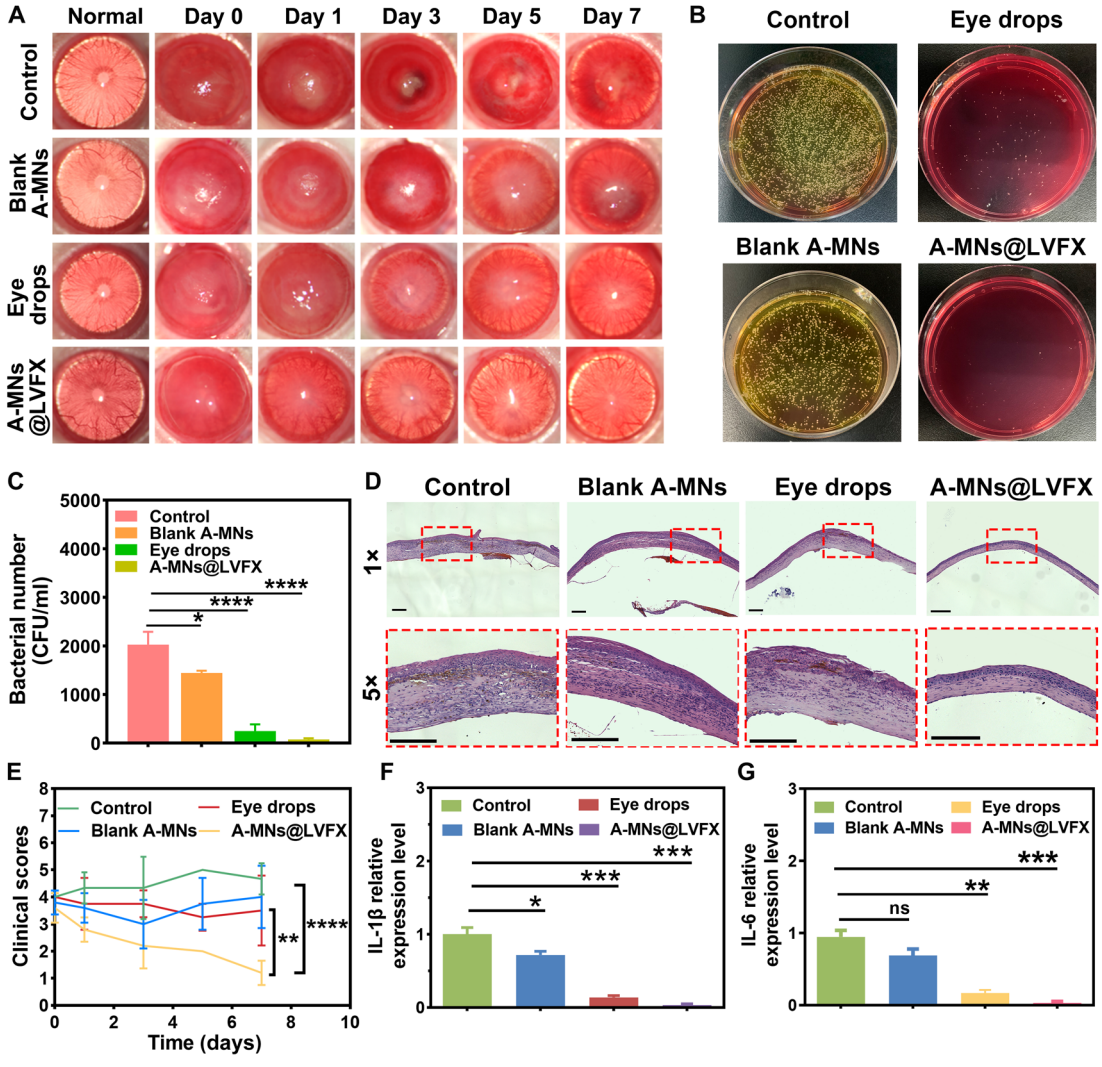

Fig. 8. Keratitis model for ocular delivery of annular microneedles (A-MNs). (**A**) The representative images of corneas by the silt lamp before and after A-MN, A-MNs@LVFX, and LVFX eye drop treatments. (**B** and **C**) The representative images and quantitative statistical analysis of *S. aureus* on the ocular surface at day 7 after different treatments. (**D**) The representative H&E staining images of corneas after different treatments. Scale bars, 200 μm. (**E**) Inflammation scores of all groups at days 0, 1, 3, 5, and 7 ($n = 3$). (**F** and **G**) IL-1β and IL-6 levels of corneas after different treatments ($n = 3$). Data are presented as means ± SD, $n \geq 3$, biological replicate, and significances are determined by one-way ANOVA with Tukey's correction. *$P < 0.05$, **$P < 0.01$, ***$P < 0.001$, and ****$P < 0.0001$.

Bacterial infection is the fundamental cause of keratitis response. Therefore, the change of bacteria number in an infected area was quantitatively measured using a plate counting method. The results showed that a large number of bacteria were present throughout the entire agar plate in the control and A-MN–treated groups (Fig. 8B). Meanwhile, there was still a certain amount of bacteria living in the LVFX eye drop–treated group. However, almost all bacteria were killed in the A-MNs@LVFX–treated group. Further statistical analysis of the number of bacteria showed a 0.52 ± 0.56 {lg [colony-forming units (CFU)/ml]} reduction in the LVFX eye drop–treated group, while a 1.27 ± 0.36 [lg (CFU/ml)] reduction of the bacteria number in the A-MNs@LVFX–treated group (Fig. 8C). Therefore, sustained release of drug from A-MNs@LVFX considerably enhanced a bactericidal effect in a corneal infection area. The observation of corneal tissue slice after H&E staining showed that a large number of inflammatory cells infiltrated the cornea in untreated and A-MN–treated groups indicating a severe inflammatory response state. Although inflammatory cell infiltration was greatly reduced in the LVFX eye drop–treated group, corneal thickness was still large indicating a state of swelling and inflammatory response. Only in the A-MNs@LVFX–treated group, inflammatory cell infiltration was much less, and corneal thickness had basically returned to normal, indicating basically disappearance of inflammatory response (Fig. 8D).

The inflammation score for quantifying an inflammatory state showed a rapid decrease in the inflammatory response in the A-MNs@LVFX–treated group during the treatment cycle, which basically returned to a normal level (Fig. 8E and table S3). Corneal thickness in the A-MN–treated group also recovered to 178.19 ± 10.34 μm on the seventh day as inflammation subsided, while corneal thickness in the eye drop–treated group was still 253.96 ± 6.65 μm (fig. S11). However, corneas were also at the visible inflammatory

response level in other three control groups. Further quantitative testing of inflammatory factors confirmed that IL-1β and IL-6 pro-inflammatory factors in the A-MNs@LVFX–treated group were significantly lower than those in the other three groups (Fig. 8, F and G). The corneal inflammatory response in the untreated group and the A-MN–treated group was more severe due the absence of a sterilization effect. The expression of two inflammatory factors in the LVFX eye drop–treated group decreased and showed a close correlation between the inflammatory response and the sterilization effect. Therefore, the minimally invasive drug delivery mode of A-MNs@LVFX achieved rapid deep corneal drug delivery, improved drug bioavailability, and a bactericidal effect.

DISCUSSION

Given the short retention time and difficulty of eye drops in penetrating into physiological barriers for ocular surface disease treatment, it has an important clinical value in the development of minimally invasive microneedle patches suitable for ophthalmic drug delivery. The ophthalmic microneedle patches in previous studies directly puncture the central cornea, which was associated with pain and reduced corneal transparency because of structural damage. In this study, a new A-MN patch drug delivery system effectively avoided damage to the central cornea and delivered drugs to an extended area of the corneal stroma layer, further spreading to the anterior cornea and the anterior chamber. First, mechanical strength for tissue puncture and suitable degradation rate were achieved through regulating the PVP-CD and PVA ratio in microneedle matrix to 1:1. It was found in in vivo corneal drug delivery experiments that bioavailability of hydrophilic drugs, hydrophobic drugs, and macromolecular protein drugs by A-MNs was increased by 24.36, 17.45, and 5.36 times, respectively, compared to the traditional eye drop administration. Furthermore, in an infectious keratitis animal experiment, LVFX-loaded A-MNs could effectively diffuse into deep corneal tissue after entering annular corneal tissue, exhibiting excellent bactericidal and inflammatory clearance effects compared to eye drops.

MATERIALS AND METHODS

Materials

Polydimethylsiloxane, PVP [K30; average molecular weight (Mw), 58 kDa], PVP (K90; average Mw, 1300 kDa), 2-hydroxypropyl β-CD, FITC, LVFX, fluorescein sodium salt, and BSA were purchased from Shanghai Aladdin Biochemical Technology (China). PVA (Mw, 27 kDa), RhB, FCZ, and Ce6 were obtained from Shanghai Macklin Biochemical Technology (China). A CCK-8 kit for mammalian cells was bought from Thermo Fisher Scientific (USA). A TUNEL apoptosis detection kit was obtained from Shanghai Yeasen Biotechnology (China). Bacteria *S. aureus* [American Type Culture Collection (ATCC) 6538] and *P. aeruginosa* (ATCC 27853) were obtained from Shanghai Luwei Technology (China). Isolated porcine eyes were obtained from farmers' market. New Zealand white male rabbits, weighing 1500 g, were provided by Danyang Changyi Experimental Animal Co. Ltd., China. Sprague-Dawley (SD) male rats (5 weeks old, weighing 150 to 180 g) and C57BL/6j mice (6 to 8 weeks old, weighing 20 to 25 g) were provided by Shanghai Jiesijie Experimental Animal Co. Ltd., China.

Preparation of microneedles

A microneedle patch was prepared by a modified micromolding method (*21*). PVP K30 and β-CD were mixed at a ratio of 1:1 to prepare PVP-β-CD solution, which was used to combine with PVA solution. The prepared PVP-β-CD/PVA mixed solution was dropped into microneedle mold to get microneedle patch. Different concentrations of PVP-β-CD and PVA were mixed in different ratios to form needle solutions at 1:1, 1:3, and 3:1. Then, the mold was put into vacuum for 30 min, and excess liquid was carefully removed. To make the base of patch, 1 ml of PVP K90 was added, and mold was put under vacuum for another 30 min. After bubbles were removed, mold was dried in a drier at 37°C to obtain an S-MN patch. A laser engraving machine (XUEGU 3020, China) was used to cut a square patch into a ring to get A-MNs. To fit different sizes of corneas, two kinds of A-MNs were prepared in this work. The A-MNs with an inner diameter of 4.5 mm and an outer diameter of 8.5 mm were made for rats, while A-MNs with an inner diameter of 6 mm and an outer diameter of 10 mm were made for rabbits and pigs. Microneedle patches containing LVFX, FCZ, Ce6, RhB, and BSA-FITC were fabricated in the same way. The prepared microneedle patches were kept in a vacuum drying tank for later use. The morphology of A-MNs was observed using field emission SEM (Hitchhi SU8010, Japan) and a stereo microscope (Cnoptec SZ650, China).

Mechanical properties of A-MNs

The mechanical strength of A-MNs in an extrusion process and the piercing into the cornea were measured by a universal material testing machine (Instron 5944, USA). The prepared A-MNs (inner diameter of 6 mm and outer diameter of 10 mm) were put on a testing bench, and the above compression probe moved down at a rate of 0.5 mm/min until it touched the tip of needles (*33*). The test began at this time, and the force bending or crushing the microneedle was recorded to draw a displacement-force curve. In the same way, porcine corneas were placed on the test bench, and A-MNs fixed on a compression probe moved down at a rate of 1.5 mm/min. The curve was recorded to explore the required force for A-MNs to penetrate into cornea. A displacement-force curve was also recorded.

Drug loading of A-MNs

The distribution of drugs in microneedles was observed using a fluorescence microscope (Leica DM4B, Germany). Four kinds of drugs including RhB, FITC, Ce6, and FITC-labeled BSA were loaded into A-MNs to represent hydrophilic drugs, hydrophobic drugs, and macromolecular drugs, respectively. In addition, the image of microneedles pierced into the rabbit cornea and dissolved in the cornea was taken using a laser confocal microscope (LSM710, Zen, Japan).

Degradation of A-MNs

The degradation of A-MNs composed of PVP-β-CD and PVA at ratios of 1:1, 1:3, and 3:1 was tested when inserted into a nutrient agar plate with water content similar to that of the cornea for different times. The fluorescence microscope (Leica DM4B, Germany) was used to photograph images of microneedles at 0, 5, 10, 15, 20, and 25 s until microneedles were completely dissolved, and the curve of microneedle height was also drawn with change of time.

In vitro drug release from A-MNs

The concentration of 3% BSA-FITC, 1% Ce6, and 0.5% FITC in precursor fluid, respectively, was used for drug-loaded A-MN preparation. The prepared A-MNs were added to a 48-well plate with 500 μl of phosphate-buffered saline (PBS) in each well. The 48-well plate was placed on the shaker to measure released drugs at different times. Then, 80 μl of liquid was taken out at 0.5, 1.5, 2.5, 3.5, 4.5, 5.5, 6.5, 8, 10, 20, and 30 min. At the same time, 80 μl of blank PBS was added to wells to keep the total amount of liquid unchanged in wells. The removed 80 μl of liquid was diluted with PBS to 400 μl. The fluorescence intensity of liquid removed at each time period was determined using a microplate reader (SpectraMax 190, Molecular Devices LLC, USA). The drug concentration was calculated according to a standard curve of drug concentration to absorbance.

In vitro antibacterial experiment

To explore drug delivery efficacy of A-MNs loading LVFX (10 mg/ml), a corneal puncture experiment was performed on isolated porcine cornea. The porcine corneas with an intact epithelium were selected and randomly divided into two groups. The drug was administered to corneas through drug-loaded A-MNs (inner diameter of 6 mm and outer diameter of 10 mm) puncture or eye drops with the same drug content. Then, corneas were placed between the recipient pool and the donor pool to simulate a fluid environment of the eye using the diffuser (TP-6, China). After 5 min, corneas were taken and washed to remove the physically adsorbed drugs. After that, corneas were grinded with a cryogenic tissue grinder (JXFSTPRP-CLN, Shanghai, China) and centrifuged at 12,000 rpm for 10 min. The corneal grinding fluid supernatant was taken for antibacterial experiments. Gram-positive *S. aureus* and Gram-negative *P. aeruginosa* were selected as model bacteria. One hundred microliters of bacterial solutions was added to a 96-well plate at a concentration of 10^5 cells/ml, and 100 μl of the supernatant stock solutions were added in each well with three parallel controls per group. After 12-hour incubation, bacterial suspensions were diluted for bacteria concentration counting.

In vivo ocular surface retention time

Rats were randomly divided into two groups for sodium fluorescein eye drops and sodium fluorescein–loaded A-MNs (inner diameter of 4.5 mm and outer diameter of 8.5 mm) treatments. In the A-MN–treated group, A-MNs loaded with 1% sodium fluorescein were pierced into corneas until completely dissolved. In the eye drop–treated group, 5 μl of 1% fluorescein sodium was administered to corneas. The presence of fluorescein sodium on the ocular surface was observed under cobalt blue mode of a slit lamp at 0, 5, 10, 15, 20, and 30 min. Images were taken, and fluorescence intensity was analyzed by ImageJ software.

In vitro corneal penetration diffusion experiment

A-MNs loaded with FITC, Ce6, and BSA-FITC were prepared as described above with the same amount of drug eye drops as control. A transdermal diffuser (TP-6) was applied to compare drug delivery efficiency of A-MNs and eye drops. The temperature was set to 37°C, and the rotation speed was set to 350 rpm. In the A-MN–treated group, porcine corneas after drug-loaded A-MN puncture were placed between the recipient pool and the donor pool, and 200 μl of PBS solution was added to the donor pool. While in the eye drop–treated group, corneas were placed in the diffuser for drug administration with 200 μl of drug solution added to the donor pool. After 5 min, the liquid in the upper donor pool was taken, and the donor pool was rinsed four times with 200 μl of PBS. The liquid and rinsing solution were collected to quantify the amount of drug that had not entered the cornea. The total amount of drugs that entered and diffused through corneas was calculated by subtracting the amount of drugs that had not entered the cornea from the total amount of drugs.

Drug distribution within the cornea

SD rats were divided into the A-MN–treated group and the free drug eye drop–treated group. The corneas were punctured by A-MNs at a concentration of 30 mg/ml of BSA-FITC, while the same amount of BSA-FITC solution was administered as eye drop. At 15, 30, and 45 min, the rat eyeball was carefully extracted in the dark. The punctured eyeball was fixed with 4% paraformaldehyde for 2 hours, and the cornea was cut off from the eyeball. Then, the corneas were made into a four-leaf clover shape by creating four radial incisions from the periphery to the center. The corneal sheet was arranged with the corneal epithelium facing up and sealed with nail polish. Last, photographs were taken using an immunofluorescence microscope. The fluorescence intensity was analyzed by ImageJ software.

Corneal structure changes after A-MN and S-MN puncture

S-MNs and A-MNs were punctured into corneas of rats to capture ocular photographs using slit lamp microscopy under bright-field and cobalt blue light modes subsequent to addition of 1% sodium fluorescein. The ocular surface was observed by microscopic morphological observation. Corneas in both groups were later extracted and dehydrated before being embedded in paraffin. Then, corneas were sliced with a microtome into slices at a thickness of 5 μm. The obtained sections were subjected to H&E staining to scrutinize histological changes of the corneal structure.

Light transmittance and corneal thickness measurement

Corneas of New Zealand white rabbits were used for light transmittance measurement. After S-MN and A-MN puncture, rabbit corneas were removed and put in phosphate buffer (PBS). Light transmittance was measured with an ultraviolet spectrophotometer (UV1780, Shimadzu). Images of corneas on a color logo, black logo, and gauze were taken using a stereo microscope (Cnopetec SZ650, China). A corneal thickness gauge (SP3000, Tomey) was used to measure the central corneal thickness before and after A-MN and S-MN puncture into rat corneas. All of the measurements were repeated three times.

Corneal nerve damage experiment

The C57BL/6j mice were divided into three groups for A-MN, S-MN, and PBS treatments. The A-MNs and S-MNs were punctured into corneas, and rat eyes were extracted and fixed with 4% paraformaldehyde for 2 hours. Afterward, incised corneas were made into four radial incisions from the periphery to the center to form a quatrefoil. Corneas were subsequently washed with PBS and immersed in a sealed permeable solution containing 5 wt % BSA and 0.5 wt % Triton X-100. After 3 hours, corneas were transferred to anti–β-III tubulin primary antibody dilution (1:500; ab52623, Abcam) and maintained at 4°C for 72 hours. Then, corneas were thoroughly washed five times with PBS and transferred into secondary antibody

dilution (1:1000; 8889S, Cell Signaling Technology) at 4°C for 24 hours. After five times washing with PBS, corneal spreads were made with an epithelial side of corneas facing up, and a cover glass was used to seal the slices. Photographs were taken using an immunofluorescence microscope, and fluorescence intensity was analyzed by ImageJ software.

Detection of pain factor expression

Both A-MNs and S-MNs were respectively inserted in rats with untreated corneas served as control. The harvested corneas were frozen and made into frozen sections for analysis after immunofluorescence staining using antibodies against COX2 (1:200; 12375-1, Proteintech) and CXCR2 (1:50; 20634-1, Proteintech). In addition, other corneas were frozen in liquid nitrogen for qPCR analysis to quantitatively evaluate the expression of IL-1β, IL-6, IL-8, and COX2 in corneas. The primers were listed in the Supplementary Materials (table S4).

In vitro biocompatibility of A-MNs

The CCK-8 cytotoxicity kit and the Live/Dead Cell Vibility/Cytotoxicity Kit were applied to test cell viability according to the manufacturer's instructions. HCECs were incubated in Dulbecco's modified Eagle's medium/F12 medium (Gibco, USA) for 48 hours and seeded in a 96-well plate at a density of 10^5 cell/ml, 100 μl per well. After cells adhered to the wall, A-MNs were added into the well, and 100 μl of new medium was added to each well for 8-hour incubation in a 5% CO_2 incubator at 37°C. Then, medium was aspirated and rinsed with PBS three times before adding 100 μl of configured CCK-8 dye to each well. After 4 hours, the absorbance at 450 nm was measured by a microplate reader (SpectraMax 190, Molecular Devices LLC, USA). Cell viability was calculated according to the following formula

$$\text{Cell viability rate (\%)} = \left(OD_{\text{A-MNs}} - OD_{\text{CCK-8}}\right) / \left(OD_{\text{Con}} - OD_{\text{CCK-8}}\right)$$

$OD_{\text{A-MNs}}$, $OD_{\text{CCK-8}}$, and OD_{Con} represent the absorbance in the A-MN–treated group, the CCK-8 dye itself, and the well only containing cells, respectively. (OD, Optical Density)

In vivo biocompatibility of A-MNs

Both in vivo H&E staining and a TUNEL cell apoptosis kit were used to evaluate the biocompatibility of A-MNs. Specifically, after 7-day treatments by S-MNs, A-MNs, and LVFX-loaded A-MNs, rat corneas were taken to make tissue paraffin sections. Paraffin sections in each group were also used for TUNEL cell apoptosis measurements according to the manufacturer's instructions. Apoptotic fragments were labeled by the dye in the kit, and cell apoptosis was observed through an upright fluorescence microscope (Leica DM4B, Germany). The remaining rats were continuously monitored for 14 days without any treatments. Eye conditions of rat corneas were recorded by a slit lamp after different treatments that were quantitatively scored according to the scoring standard (table S2). Corneas of rats were removed for qRT-PCR analysis to measure IL-1 and TNF-α expression. The primers were listed in the Supplementary Materials (table S4). The rat corneas were divided into superior, inferior, nasal, and temporal quadrants to obtain the sodium fluorescein staining score by adding scores of four quadrants according to Christophe Baudouin's and other standards (*31*, *34*). Then, the expression of α-SMA was also measured after immunofluorescence staining (1:2000; 14395-1, Proteintech).

Infectious keratitis model establishment and treatment

The animal experimental research was approved by Experimental Animal Ethics Review Committee of Wenzhou Medical University. All experimental animals were kept in the Experimental Animal Center of Wenzhou Medical University, which met the requirements of Conduct for Care Code and Use of Experimental Animals (license number: wydw2021-0332). All animals were bred adaptively for 1 week before experiments.

The rats were randomly divided into four groups for PBS, A-MNs, A-MNs@LVFX, and LVFX eye drop treatments. The inner and outer diameters of 4.5 and 8.5 mm, respectively, of A-MNs were applied in the experiments. The corneal epithelium of rats in each group was scraped off under anesthesia and was covered with a filter paper containing bacterial solution (*S. aureus*, 1×10^8 CFU/ml) with eyelids sutured. After 24 hours, corneas were observed under a slit lamp to examine corneal inflammation. The A-MN and A-MNs@LVFX patches were punctured into the peripheral cornea by manual pressing. The LVFX eye drops were administered twice a day, which was consistent with clinical application. The control group did not receive any treatments. On days 1, 3, 5, and 7 after treatments, recovery of corneal inflammation was observed under a slit lamp, and the inflammation score was performed according to modified Peyman's criteria (table S3) (*35*, *36*). The corneal thickness of rats in each group was measured on days 1, 3, and 7. The corneas of rats in each group were randomly removed to measure corneal transparency by an ultraviolet spectrophotometer (UV1780, Shimadzu) on days 1, 3, and 7 of each group. All of the animals were sent to the Experimental Animal Center for unified treatment after experiments.

Histology analysis and qRT-PCR analysis

Corneas of rats were taken after 7-day treatments. The removed eyes were quickly cut off from euthanized rats after fixation under low temperature conditions. The slices of corneas were stored in liquid nitrogen for later use. Tissue sections were stained with H&E to observe the structures of corneas. qRT-PCR was performed to verify the expressions of inflammatory factors IL-1β and IL-6. According to the manufacturer's instructions, total RNA was extracted from a single whole cornea and quantified by spectrophotometry (260 nm). Then, 1 μg of RNA was reverse-transcribed into cDNA by the PrimeScriptTM RT reagent Kit (TaKaRa, Japan). After that, PCR analysis of IL-1β and IL-6 was performed by SYBR Green PCR Master Mix (Applied Biosystems, Foster City, CA, USA). The primers were listed in the Supplementary Materials (table S4).

Statistical analysis

All of the experiments were conducted in triplicate, and the data presented in this paper were as mean ± SD. Statistical analysis between the two groups was performed using the one-way analysis of variance (ANOVA). Statistical significance was assumed at $^*P < 0.05$, $^{**}P < 0.01$, $^{***}P < 0.\,001$, and $^{****}P < 0.\,0001$.

Supplementary Materials

This PDF file includes:

Figs. S1 to S11

Tables S1 to S4

REFERENCES AND NOTES

1. S. R. Flaxman, R. R. A. Bourne, S. Resnikoff, P. Ackland, T. Braithwaite, M. V. Cicinelli, A. Das, J. B. Jonas, J. Keeffe, J. H. Kempen, J. Leasher, H. Limburg, K. Naidoo, K. Pesudovs, A. Silvester, G. A. Stevens, N. Tahhan, T. Y. Wong, H. R. Taylor, Global causes of blindness and distance vision impairment 1990–2020: A systematic review and meta-analysis. *Lancet* **5**, e1221–e1234 (2017).
2. M. Singh, S. Bharadwaj, K. E. Lee, S. G. Kang, Therapeutic nanoemulsions in ophthalmic drug administration: Concept in formulations and characterization techniques for ocular drug delivery. *J. Control Release* **328**, 895–916 (2020).
3. L. J. Luo, D. D. Nguyen, J. Y. Lai, Dually functional hollow ceria nanoparticle platform for intraocular drug delivery: A push beyond the limits of static and dynamic ocular barriers toward glaucoma therapy. *Biomaterials* **243**, 119961 (2020).
4. D. Huang, Y. S. Chen, I. D. Rupenthal, Overcoming ocular drug delivery barriers through the use of physical forces. *Adv. Drug Deliv. Rev.* **126**, 96–112 (2018).
5. C. Wang, Y. Pang, Nano-based eye drop: Topical and noninvasive therapy for ocular diseases. *Adv. Drug Deliv. Rev.* **194**, 114721 (2023).
6. P. Argueso, Human ocular mucins: The endowed guardians of sight. *Adv. Drug Deliv. Rev.* **180**, 114074 (2022).
7. Y. Chen, Z. Ye, H. Chen, Z. Li, Breaking barriers: Nanomedicine-based drug delivery for cataract treatment. *Int. J. Nanomedicine* **19**, 4021–4040 (2024).
8. N. Nagai, H. Otake, Novel drug delivery systems for the management of dry eye. *Adv. Drug Deliv. Rev.* **191**, 114582 (2022).
9. A. Urtti, L. Salminen, Minimizing systemic absorption of topically administered ophthalmic drugs. *Surv. Ophthalmol.* **37**, 435–456 (1993).
10. X. Yuan, D. C. Marcano, C. S. Shin, X. Hua, L. C. Isenhart, S. C. Pflugfelder, G. Acharya, Ocular drug delivery nanowafer with enhanced therapeutic efficacy. *ACS Nano* **9**, 1749–1758 (2015).
11. R. B. Singh, S. Das, J. Chodosh, N. Sharma, M. E. Zegans, R. P. Kowalski, V. Jhanji, Paradox of complex diversity: Challenges in the diagnosis and management of bacterial keratitis. *Prog. Retin. Eye Res.* **88**, 101028 (2022).
12. T. Y. Kim, G. H. Lee, J. Mun, S. Cheong, I. Choi, H. Kim, S. K. Hahn, Smart contact lens systems for ocular drug delivery and therapy. *Adv. Drug Deliv. Rev.* **196**, 114817 (2023).
13. T. Lajunen, R. Nurmi, L. Kontturi, L. Viitala, M. Yliperttula, L. Murtomaki, A. Urtti, Light activated liposomes: Functionality and prospects in ocular drug delivery. *J. Control Release* **244**, 157–166 (2016).
14. M. Rafat, M. Xeroudaki, M. Koulikovska, P. Sherrell, F. Groth, P. Fagerholm, N. Lagali, Composite core-and-skirt collagen hydrogels with differential degradation for corneal therapeutic applications. *Biomaterials* **83**, 142–155 (2016).
15. W. Li, R. N. Terry, J. Tang, M. H. R. Feng, S. P. Schwendeman, M. R. Prausnitz, Rapidly separable microneedle patch for the sustained release of a contraceptive. *Nat. Biomed. Eng.* **3**, 220–229 (2019).
16. Q. Chen, Z. Xiao, C. Wang, G. Chen, Y. Zhang, X. Zhang, X. Han, J. Wang, X. Ye, M. R. Prausnitz, S. Li, Z. Gu, Microneedle patches loaded with nanovesicles for glucose transporter-mediated insulin delivery. *ACS Nano* **16**, 18223–18231 (2022).
17. R. Jamaledin, C. K. Y. Yiu, E. N. Zare, L. N. Niu, R. Vecchione, G. Chen, Z. Gu, F. R. Tay, P. Makvandi, Advances in antimicrobial microneedle patches for combating infections. *Adv. Mater.* **32**, e2002129 (2020).
18. J. You, C. Yang, J. Han, H. Wang, W. Zhang, Y. Zhang, Z. Lu, S. Wang, R. Cai, H. Li, J. Yu, J. Gao, Y. Zhang, Z. Gu, Ultrarapid-acting microneedles for immediate delivery of biotherapeutics. *Adv. Mater.* **35**, e2304582 (2023).
19. K. Glover, D. Mishra, S. Gade, L. K. Vora, Y. Wu, A. J. Paredes, R. F. Donnelly, T. R. R. Singh, Microneedles for advanced ocular drug delivery. *Adv. Drug. Deliv. Rev.* **201**, 115082 (2023).
20. Y. Wang, P. Guan, R. Tan, Z. Shi, Q. Li, B. Lu, E. Hu, W. Ding, W. Wang, B. Cheng, G. Lan, F. Lu, Fiber-reinforced silk microneedle patches for improved tissue adhesion in treating diabetic wound infections. *Adv. Fiber Mater.* **6**, 1596–1615 (2024).
21. A. Than, C. Liu, H. Chang, P. K. Duong, C. M. G. Cheung, C. Xu, X. Wang, P. Chen, Self-implantable double-layered micro-drug-reservoirs for efficient and controlled ocular drug delivery. *Nat. Commun.* **9**, 4433 (2018).
22. M. W. Ansari, A. S. Nadeem, "Transparent structures of the eyeball cornea, lens, and vitreous" in *Atlas of Ocular Anatomy* (Springer, 2016), pp. 65–70.
23. J. L. Alió del Barrio, A. De la Mata, M. P. De Miguel, F. Arnalich-Montiel, T. Nieto-Miguel, M. El Zarif, M. Cadenas-Martín, M. López-Paniagua, S. Galindo, M. Calonge, J. L. Alió, Corneal regeneration using adipose-derived mesenchymal stem cells. *Cells* **11**, 2549 (2022).
24. A. J. Rózsa, R. W. Beuerman, Density and organization of free nerve endings in the Cornea1 epithelium of the rabbit. *Pain* **14**, 105–120 (1982).
25. E. Zander, G. Weddell, Observations on the Innervations of the Cornea. *J. Anat.* **85**, 68–99 (1951).
26. S. P. Mariotti, Global data on visual impairments. *World Health Organization 2012*, (2010).
27. W. Park, V. P. Nguyen, Y. Jeon, B. Kim, Y. Li, J. Yi, H. Kim, J. W. Leem, Y. L. Kim, D. R. Kim, Y. M. Paulus, C. H. Lee, Biodegradable silicon nanoneedles for ocular drug delivery. *Sci. Adv.* **8**, eabn1772 (2022).
28. J. He, H. E. Bazan, Mapping the nerve architecture of diabetic human corneas. *Ophthalmology* **119**, 956–964 (2012).
29. K. Liu, L. Wu, S. Yuan, M. Wu, Y. Xu, Q. Sun, S. Li, S. Zhao, T. Hua, Z. J. Liu, Structural basis of CXC chemokine receptor 2 activation and signalling. *Nature* **585**, 135–140 (2020).
30. T. Das, J. Joseph, M. P. Simunovic, A. Grzybowski, K. J. Chen, V. P. Dave, S. Sharma, P. Staropoli, H. Flynn Jr., Consensus and controversies in the science of endophthalmitis management: Basic research and clinical perspectives. *Prog. Retin. Eye Res.* **97**, 101218 (2023).
31. R. Qin, Y. Guo, H. Ren, Y. Liu, H. Su, X. Chu, Y. Jin, F. Lu, B. Wang, P. Yang, Instant adhesion of amyloid-like nanofilms with wet surfaces. *ACS Cent. Sci.* **8**, 705–717 (2022).
32. S. Kenchegowda, H. E. Bazan, Significance of lipid mediators in corneal injury and repair. *J. Lipid Res.* **51**, 879–891 (2010).
33. G. Roy, R. D. Galigama, V. S. Thorat, L. S. Mallela, S. Roy, P. Garg, V. V. K. Venuganti, Amphotericin B containing microneedle ocular patch for effective treatment of fungal keratitis. *Int. J. Pharm.* **572**, 118808 (2019).
34. A. Pauly, F. Brignole-Baudouin, A. Labbe, H. Liang, J. M. Warnet, C. Baudouin, New tools for the evaluation of toxic ocular surface changes in the rat. *Invest. Ophthalmol. Vis. Sci.* **48**, 5473–5483 (2007).
35. H. Guo, J. Gao, X. Wu, Toll-like receptor 2 siRNA suppresses corneal inflammation and attenuates aspergillus fumigatus keratitis in rats. *Immunol. Cell. Biol.* **90**, 352–357 (2012).
36. M. L. Durand, M. B. Barshak, J. Chodosh, Infectious keratitis in 2021. *JAMA Ophthalmol.* **326**, 1319–1320 (2021).

Acknowledgments

Funding: This work was supported by the Zhejiang Provincial Natural Science Foundation of China (LR21H180001), National Natural Science Foundation of China (82072077), and Zhejiang Provincial Traditional Chinese Medicine Science and Technology Project (2021ZA091), which are greatly acknowledged. **Author contributions:** L.W., Y.G., Y.J., and B.W. designed the experiments. L.W., Y.G., B.C., S.L., J.Y., Y.J., X.W., X.S., and S.W. performed the experiments and collated the data. L.W., B.C., S.L., and Y.G. analyzed the data. L.W., Y.G., and B.W. wrote the paper. **Competing interests:** The authors declare that they have no competing interests. **Data and materials availability:** All data needed to evaluate the conclusions in the paper are present in the paper and/or the Supplementary Materials.

Submitted 7 December 2024
Accepted 31 January 2025
Published 7 March 2025
10.1126/sciadv.adv1661